Journal of Marine Science and Application (2026) 25: 1-14
https://doi.org/10.1007/s11804-025-00708-2

RESEARCH ARTICLE

Fluid Forces on a Hydrofoil for Kitefoil and Windfoil Boards: Experimental Investigation on Their Dependence on the Froude Number Based on Submergence

H. Martínez-Barberá[1,2], J. Calderon-Sanchez[3], L. Moulian[4] and A. Souto-Iglesias[3]

Received: 12 September 2024 / Accepted: 20 April 2025

Abstract

Races using kitefoil and windfoil surfboards have been in the Olympic Games for the first time in Paris 2024, signalling their relevance in sailing sports. However, the dynamics of these devices is yet not well understood, in particular the influence on the hydrodynamic forces and moments of the distance of the foil to the free surface. Considering this, the present paper documents an experimental investigation in which forces and torque produced, under uniform flow, by a full-scale state-of-the-art hydrofoil (suitable both for kitesurf and windsurf) were measured. A range of velocities, angles of attack, and submergences were tested, leading to Froude numbers based on submergence with maximum values around five, a typical range in actual sailing conditions. From these tests, formulae for the hydrodynamic coefficients have been proposed. They can be used for developing Velocity Prediction Programs (VPP) for this kind of craft, a necessary tool to plan racing configurations and to analyze their racing performance. With the aim of making the experimental data useful for benchmarking numerical models and for future research on related topics such as foil ventilation and transition to turbulence, the specimen's 3D file is provided as supplementary material to this paper.

Keywords Hydrofoil; Kitefoil; Windfoil; Velocity prediction programs; Lift coefficient; Drag coefficient

1 Introduction

Currently, the use of hydrofoils in recreational crafts is an established trend in a growing market with many different products available. Within the range of recreational hydrofoil boards, this paper focuses on those for use in hydrofoil-based kitesurf (kitefoil) and windsurf (windfoil) boards. However, the results presented can also be useful for other types of boards, such as wingfoil and surffoil boards.

All these kinds of boards are based on a submerged surface that generates lift to overcome the weights of the rider and the board itself (see Figure 1). Hence, this force can push and maintain the board over the water surface, greatly minimizing both friction and wave resistance. Consequently, large navigation speeds can be achieved easily, even in light wind conditions (up to 6 knots for large surface area hydrofoils), thus expanding the range of locations in which these activities can be practiced.

Today, there is such a growing economic interest in these activities that it is expanding the types of foils available. Nevertheless, research oriented towards better designs is scarce and limited to riders' experience and very simple hydrodynamic theories. In fact, the experimental literature on the hydrodynamics of such equipment is missing, as far as the authors are aware, a fact that motivates this research.

The foil technology permeated into the sailing boat industry in 1950 when G. Baker was able to sail in a dinghy with hydrofoils at a speed of 20 knots. Later in 1956 he reached 30.4 knots in his dinghy Monitor (currently on display in the Small Craft Collection at the Mariners' Museum, 100 Museum Drive, Newport News, Virginia, USA).

As discussed in the reviews of Tisserand (2005) and Vellinga (2009), following Baker's opened path, in the 1960s

Article Highlights

- Experimental investigation in which fluid forces and torque produced by a state-of-the-art hydrofoil were measured.
- A range of velocities, angles of attack, and submergences were tested, with Froude numbers based on submergence with maximum values around 5, a typical range in actual sailing conditions.
- Formulae for the hydrodynamic coefficients have been proposed that can be used in VPPs for kitefoils as first estimation.
- The specimen's 3D file is provided as supplementary material to this paper for validation purposes.

✉ A. Souto-Iglesias
antonio.souto@upm.es

[1] DIIC, Facultad de Informática, Universidad de Murcia, Murcia 30100, Spain

[2] ETSIN, Universidad Politécnica de Madrid (UPM), Madrid 28040, Spain

[3] CEHINAV, DACSON, ETSIN, Universidad Politécnica de Madrid (UPM), Madrid 28040, Spain

[4] SeaTech, Université de Toulon, La Garde 83130, France

(a) Kitefoil board (Source: Gisela pulido)

(b) Windfoil board (Source: Pilar lamadrid, Photo: Sailing energy)

Figure 1 Actual hydrofoils in operation

and the 1970s more developments appeared on small hydrofoil supported sailing boats. Indeed, through the work of some pioneers like D. J. Nigg and D. Keiper in the USA, P. Hansford and J. Grogono in the UK, and C. Tisserand and E. Tabarly in France, a substantial increase in the speed of such boats was achieved during these years.

In the early 2000s the hydrofoil adventure became mature with the emergence of the ORMA 60 foil-assisted trimarans and personal dinghies like the moth foiler. The International Moth class experienced a resurgence of interest and publicity associated with the adoption of hydrofoils, and nowadays is one of the most profitable hydrofoil sailing classes. In this context, several experimental investigations have been carried out to improve the performance of various types of hydrofoil crafts (Binns et al., 2008; Beaver and Zseleczky, 2009; Barden and Binns, 2012; Campbell et al., 2014; Souppez et al., 2019; Day et al., 2019; Giallanza et al., 2020; Vanilla et al., 2021; Marimon Giovannetti et al., 2022).

Hydrofoil technology has lately gained popularity thanks to its inclusion in some of the most prominent racing regattas. Hydrofoils were first included in the AC72 catamarans for the 2013 America's Cup, and they have been later expanded to other competitions such as SailGP (which are adapted from the AC50 boats of the 2017 America's Cup) or the Ocean Race and Vendée Globe, based on IMOCA-60 yachts equipped with hydrofoils. All these examples demonstrate that match racing regattas are possible for foiling yachts, increasing attention on this technology and stimulating the development of many other hydrofoil-based crafts. An indication of these trends is the incorporation of the Formula Kite and the Starboard iQFOiL (see Figure 1) as Olympic classes in the 2024 Games.

The aim of this work is to experimentally assess the influence of the angle of attack and submergence below the water surface on the performance of a board-based hydrofoil. Similar experimental studies have been performed in the past on rectangular planform hydrofoils of high aspect ratio (Wadlin et al., 1950; Carter and Butler, 1953; Wadlin et al., 1955; Daskovsky, 2000; Ni et al., 2021; Jentzsch et al., 2022; Wang et al., 2023).The focus is however here on the Froude number based on submergence, which is useful to extend the results to higher speed, as well as on complex configurations (low aspect ratios, non-prismatic wings and multiple wings), common of present state-of-the-art hydrofoils for kite and windsurf boards. More specifically, the following questions will be studied: first, characterize the dependence of the hydrodynamic coefficients on the foil's angle of attack, speed, and Froude number based on submergence; second, when possible, these results will be compared with available literature; third, simplified models for these hydrodynamic coefficients will be proposed, that can be used in Velocity Prediction Program (VPP) codes.

The structure of the paper is organized as follows: First, the specimen studied is presented. Second, the experimental setup is discussed. Following this, test matrix is proposed, and experimental results are presented, discussed, and simplified models are provided. Finally, conclusions are outlined and suggestions for future research are established.

2 Case study

The model used in this work is depicted in Figure 2. It is the same design that was analyzed numerically in Ocaña Blanco et al. (2017). Its CAD file is provided as supplementary material in this link: https://mega.nz/folder/uBxzhLKa#Y45F_r73wH5yQ6JWRg_VeA, in order for other researchers to validate their numerical results. Some sample videos of the experiments can also be accessed from the same link. The design was developed by Wolfgang Habe from Polymer Technology SL, Spain, who used the results of the present campaign and previous numerical modeling (Ocaña Blanco et al., 2017) for improving a recent commercial one-crew sail foil boat, Mothquito (https://www.mothquito.com/). The specimen is constructed with carbon fiber reinforced and epoxy resins. As is usual on these boards, it consists of four elements (as shown in Figure 2:

• A main wing, responsible for the generation of most of the lifting force,

• a rear wing that acts as a stabilizer and controls lifting surface,

• a mast that serves as the lifting surface to minimize leeway,

• a fuselage that acts as a mechanical connection between the previous elements.

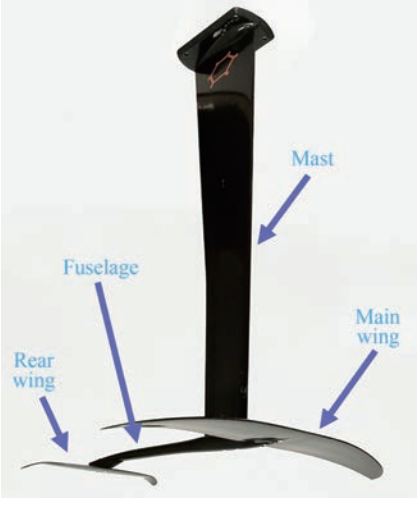

Figure 2 Full scale case study specimen. Polymer-Technology SL®

The configuration of the submerged elements resembles that of a conventional aircraft. The main wing provides most of the vertical lift in the same fashion as the wing of an airplane. The rear wing acts as a control surface to guarantee longitudinal stability. The mast contributes by generating the lateral force needed to reduce the leeway angle when sailing upwind. In some sailing configurations, which are not covered in this paper, the hydrofoil operates with an attitude (α, β, γ) that couples the lift produced by its different surfaces. This happens, for instance, when sailing upwind with some leeway angle and windward heeling angle (as appreciated in both panels of Figure 1).

Both the main and rear wings are built from a non-symmetric section, since they need to generate lift mainly in one direction to push the board out of the water even at low angles of attack (Figures 3 and 4). The main wing section is derived from the NACA 63-210 profile, and the rear wing section is based on the NACA 63-209 profile. Given that the function of the mast is to counteract the leeway that may be induced, a symmetric NACA 0009 section (Figure 5) is used so that it can generate lift equally in both directions.

Figure 3 Main foil section. NACA 63-210 (non-symmetric)

Figure 4 Rear foil section. NACA 63-209 (non-symmetric)

Figure 5 Mast section. NACA 0009 (symmetric)

The dimensions and main parameters for all four elements are presented in Table 1, same as in the work by Ocaña Blanco et al. (2017). Hence, reference geometric values used to present forces and moments in non-dimensional form are taken from this table. The mast dimensions are shown in a sketch in Figure A2 in Appendix A.

Table 1 Main dimensions of the case study specimen. Same values as in Ocaña Blanco et al. (2017) are used

Main foil		
Planform surface (S)	0.0590 m^2	
Wingspan (b)	0.6340 m	
Mean chord (c)	0.0735 m	
Effective span, $\left(b_{\text{eff}} \coloneqq S/c\right)$	0.8027 m	
Aspect ratio, $\left(\text{AR} \coloneqq b_{\text{eff}}/c\right)$	10.92	
Thickness (t)	10% of c	
Geometric angle of attack (AOA) (α_0)	2°	
Rear foil		
Planform surface (S_r)	0.0210 m^2	S_r/S = 0.36
Wingspan (b_r)	0.3420 m	b_r/b = 0.54
Mean chord (c_r)	0.0435 m	c_r/c = 0.59
Thickness (t_r)	9% of c_r	
Geometric AOA (α_0)	0°	
Mast		
Planform surface (S_k)	0.1283 m^2	S_k/S = 2.17
Wingspan (b_k)	0.8890 m	b_k/b = 1.40
Mean chord (c_k)	0.1125 m	c_k/c = 1.53
Thickness (t_k)	9% of c_k	
Fuselage		
Lateral surface (S_f)	0.0137 m^2	S_f/S = 0.23
Length (L_f)	0.5920 m	L_f/b = 0.93
Width (b_f)	0.0351 m	b_f/b = 0.06
Height (t_f)	0.0301 m	t_f/b = 0.05

Although the results obtained in this paper are for a specific design, it can be assumed that the general conclusions derived from this work may also be applicable in a general context, provided that the design tested here is representative of others available on the market (see Ocaña Blanco et al. (2017), where a number of representative designs are displayed).

3 Experimental setup

3.1 System of reference

Understanding the full hydrofoil's hydrodynamics would require analyzing the flow in all possible directions, including the influence of all the different angles between the flow and the board, namely: angle of attack (α), leeway angle (β) and heel angle (γ). However, in this paper, only the experiments changing the α values have been considered.

Two reference frames are defined at this point to help the explanations that follow and the analysis of the results in the foregoing sections: a frame fixed to the body, known as the body frame, and a frame linked to the hydrodynamic velocity known as the water frame. The orientation between these two reference systems defines the three angles previously mentioned. These reference frames are shown in Figure 6 and described next.

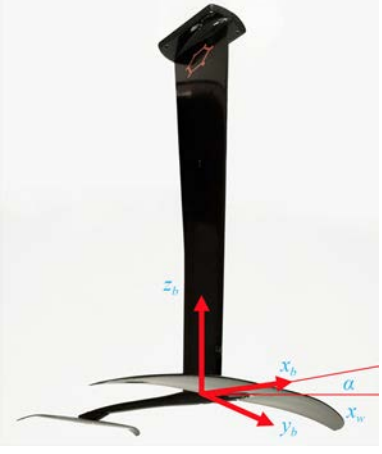

Figure 6 Body frame (x_b, y_b, z_b) defined in a hydrofoil device, with respect to a water frame (x_w, y_w, z_w). Only α rotations with respect to the y_w axis have been considered in this studied

• Body frame. The x_b axis is positive out the nose of the hydrofoil in the plane of symmetry of the device, the z_b axis is perpendicular to the x_b axis, at plane of symmetry, positive upwards, and the y_b axis is perpendicular to the previous ones, positive determined by the right-hand rule. The origin of the body frame O_b is assumed at the intersection of the mast axis and the fuselage. The mast axis is assumed to run in the center plane of the mast and passes through the center of the chord of the mast tip (see sketches in Figures A2–A5 in Appendix A, where the points where the torques were measured are also clearly identified).

• Water frame. Its origin O_w coincides with the origin of the body frame O_b. The x_w axis is positive in the direction of the incoming velocity at each moment, the z_w axis is perpendicular to the x_w axis, positive upwards and the y_w axis is perpendicular to the previous ones, its positive direction determined by the right-hand rule. A detailed explanation of the reference frames and the orientation between them can be found in Gómez et al. (2012).

3.2 Facility and equipment

The experiments were conducted in CEHINAV ETSIN-UPM towing tank, which has the following dimensions: Depth = 2.2 m, Width = 3.8 m, and Length = 100 m. A view of the facility is shown in Figure 7.

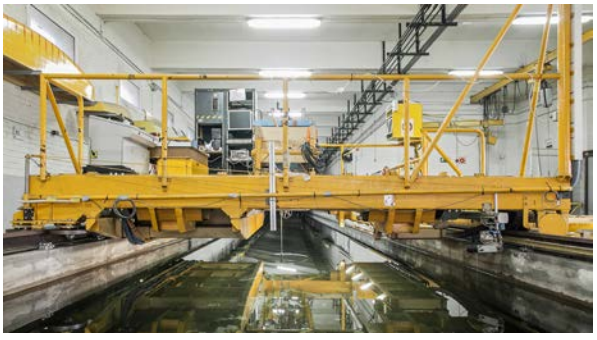

Figure 7 Carriage in towing tank; hydrofoil visible

The hydrofoil model was fixed to the carriage, which has a maximum speed of 4.0 m/s. The velocity of each run is programmed beforehand, and the carriage has an automatic speed control that keeps it constant.

Figure 8 shows how the specimen was fixed to the carriage. The connection includes a mechanism composed of two vertical bars joined to a platform which allows moving elements connected to it vertically, with a precision of ±0.5 mm, through the use of a worm gear (left panel of Figure 9).

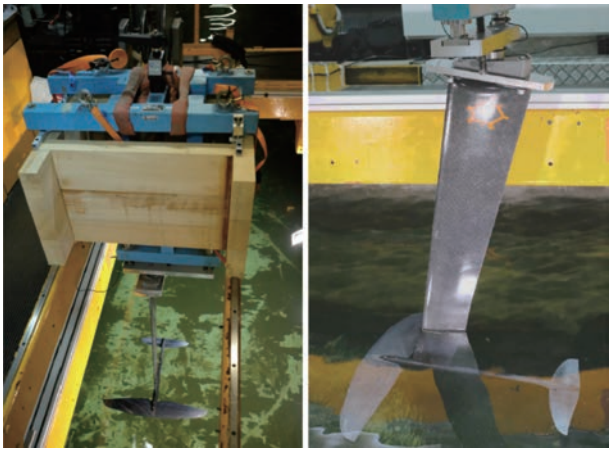

Figure 8 Fixation of specimen to the towing carriage

An aluminum plate was bolted to the previously described mechanism and a 6-DOF force and torque sensor was ingrained into the lower surface of this plate. This transducer was bolted by its bottom to a wedge (Figure 10), built of high-density polyurethane or aluminum, responsible for providing the attitude. Finally, another aluminum plate

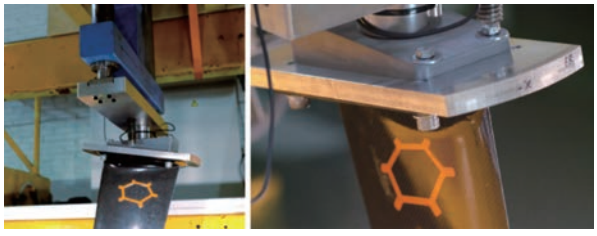

Figure 9 Load cell fixation

Figure 10 Wedges, from left to right: first, corresponds to $\alpha = 5°$, $\beta = 30°$, $\gamma = 0°$; then, variations are for angle α only: 1.25°, 2.5°, 20°, 5° and 10°

bolted to the wedge was used to screw the specimen. This setup can be seen in Figure 9 and the wedges in Figure 10.

The same wedges were also used for negative cases.

The results regarding the forces will be given in the water frame of reference, and the moments will be given at the base of the specimen, where it is clamped to the board. The coordinates of this point for the various angles of attack are given in the water frame of reference, in Figures A2–A5 in Appendix A).

4 Results

Flow conditions depend on a set of non-dimensional numbers: Reynolds number, Froude number based on the chord, Froude number based on submergence, and submergence ratio. They are defined, respectively:

$$Re = \frac{\rho u_\infty c}{\mu}, \quad Fr_c = \frac{u_\infty}{\sqrt{gc}}, \quad Fr_h = \frac{u_\infty}{\sqrt{gh}}, \quad h_c = \frac{h}{c} \quad (1)$$

In the previous expressions, u_∞ is the flow velocity, ρ and μ the fluid density and dynamic viscosity, respectively, g the gravity acceleration, h the submergence referred to the water frame of reference origin O_w. The three latter equations in Eq. (1) are not independent as:

$$Fr_h = \frac{Fr_c}{\sqrt{h_c}} \quad (2)$$

The goal of the experimental campaign is to measure the hydrodynamic loads (forces and moments) exerted on the test specimen for different angles of attack (α), while varying the flow conditions: Froude numbers Fr_h and Fr_c, and submergence ratio (h_c). Table 2 shows the α cases tested that are of interest for this paper and whose variations are intended to describe the polar curves until the onset of stall conditions. For this range of angles of attack, flow conditions include speeds 1 m/s $\leqslant u_\infty \leqslant$ 4 m/s and submergences $0.5 \leqslant h_c \leqslant 9.5$, equivalent to $0.4 \leqslant Fr_h \leqslant 6.7$ and $1.2 \leqslant Fr_c \leqslant 4.7$.

Table 2 Angles of attack considered in the experimental campaign

α (°)							
−5.0	−2.5	−1.25	0.0	1.25	2.5	5.0	10

One main objective of this paper is to create a model of the non-dimensional coefficients for lift, drag, and moment so that they can be incorporated in a VPP taking into account the flow conditions. The force coefficient C_i in the $i = 1, 2, 3$, corresponding to x, y, z directions, respectively, is defined as

$$C_i = \frac{F_i}{\frac{1}{2}\rho u_\infty^2 S} \quad (3)$$

with F_i being the measured force in the i direction, ρ the water density, u_∞ the speed, and S the planform surface (see Table 1).

Coefficient of moment around the y axis, C_m, is also studied, defined in the equation

$$C_m = \frac{M_2}{\frac{1}{2}\rho u_\infty^2 Sc} \quad (4)$$

with M_2 being the y moment, and c the mean chord of the main wing (see Table 1).

In order to check for dependencies, using dimensional analysis, the coefficients can be shown to be a function of the non-dimensional quantities involved:

$$C_{[\cdot]} = C_{[\cdot]}\left(\alpha, \beta, \gamma, h_c, Re, Fr_h\right) \quad (5)$$

Focusing on a particular specimen, since the kinematic viscosity of salt and fresh water are rather similar, Re is proportional to Fr_h/h_c, it can be dropped from Eq. (5). In addition, since only varying the α angle has been considered in this study, both β and γ can be dropped as well, leading to:

$$C_{[\cdot]} = C_{[\cdot]}\left(\alpha, h_c, Fr_h\right) \quad (6)$$

The strategy to determine these functional relationships for the $C_{[\cdot]}$ functions is to conduct two batches of experiments:

• A first batch of experiments aim to find the relationship of the exerted hydrodynamic forces and moments with respect to the angle of attack (α) and flow velocity (u_∞), while maintaining submergence (h_c) at its maximum depth. The experimental conditions are: $-5° \leqslant \alpha \leqslant +10°$, 1 m/s $\leqslant u_\infty \leqslant$ 4 m/s, and $h_c = 9.5$. Reynolds number of the tests are in the range of $7.3 \times 10^4 \leqslant Re \leqslant 2.9 \times 10^5$, which correspond to $0.4 \leqslant Fr_h \leqslant 1.5$.

• A second batch of experiments aims to find the relationship of the exerted hydrodynamic forces and moments with respect to the angle of attack (α) and flow submergence (h_c), while maintaining the velocity (u_∞) at its maximum value, the closest to the actual typical sailing conditions that can be reached in the facility. The experimental conditions are $-5° \leqslant \alpha \leqslant +10°$, $0.5 \leqslant h_c \leqslant 9.5$, and $u_\infty = 4$ m/s, which correspond to $1.5 \leqslant Fr_h \leqslant 6.7$.

In the following subsections, mathematical expressions for the coefficients with the dependencies indicated in Eq. (6) will be developed. Steady-state conditions are the focus of the present paper, though in actual operation transient lift forces can be of interest, for instance for maneuvering of sailing yachts in waves (Angelou and Spyrou, 2019).

4.1 Dependence on the velocity

Operational speeds are of the order of 10 m/s while the maximum carriage speed of the tank is 4 m/s. The question arises whether the speed is high enough so that there is little dependence on the Reynolds number on the coefficients ($Re = 2.9 \times 10^5$ at 4 m/s and $Re = 7.3 \times 10^5$ at 10 m/s). To investigate this question, data from the first batch of experiments has been non-dimensionalized, and drag, lift, and moment coefficients have been obtained for a range of angles of attack α, and a velocity u_∞ for large submergence ratios $h_c \geqslant 5$. For this range of submergences, free surface effects are expected to be negligible for these speeds, which would affect their assessment. The results are presented in Figure 11.

It can be seen that the lift and drag coefficients tend to reach rather constant values for velocities $u_\infty \geqslant 3.5$ m/s. For this reason, only the velocities in the range $3.5 \text{ m/s} \leqslant u_\infty \leqslant 4$ m/s, ($2.5 \times 10^5 \leqslant Re \leqslant 2.9 \times 10^5$) will be used in the analyses in the paper.

Even with this evidence on practical Reynolds independence of the results in a certain range, taken as the one of interest, the issue of transition to turbulence deserves some comment. Indeed, specific tests using turbulence stimulators to trigger transition were carried out. However, for the present paper, to contain its length and to make the case study definition simpler, only the canonical configuration for the foil, without any modification, has been considered. In the future, it would be interesting to conduct numerical analysis focusing on determining critical Reynolds number for the NACA 63-210. It is a difficult problem, expected to be even harder to model due to hydroelastic effects and minor vibrations induced by the carriage.

To close this section, it can be interesting to give an example in dimensional terms. For instance, for $\alpha = 5°$, $h_c = 4$ and $u_\infty = 3.5$ m/s, the lift force is equal to 283 N, the drag force is equal to 36 N and the pitch moment is equal to 50 N·m. Doubling the speed, the lift force will approximately reach 120 kg, more than enough to sustain the rider and the craft.

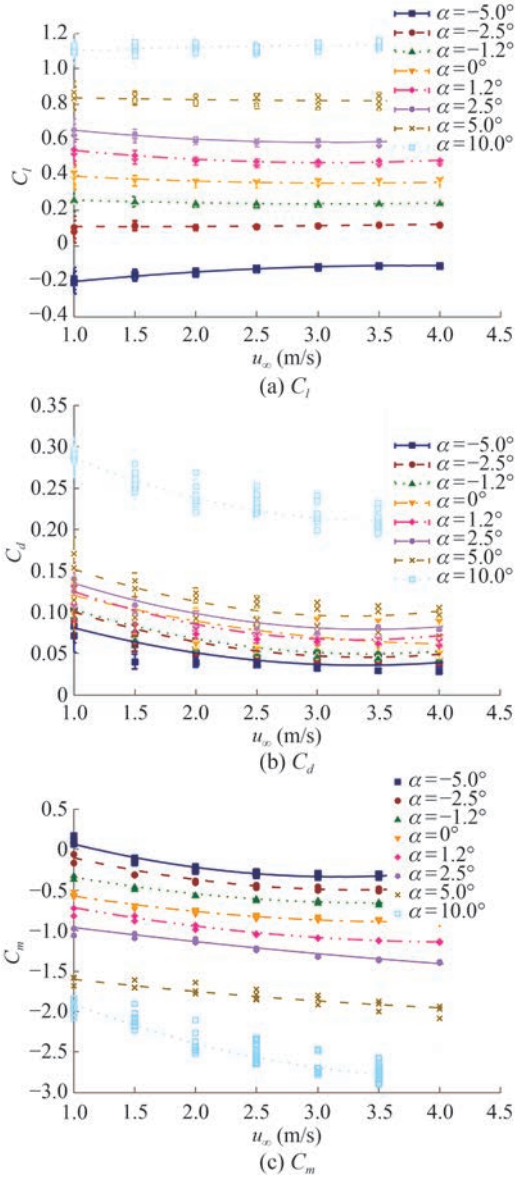

Figure 11 Coefficients for varying α and u_∞, $h_c \geqslant 5$

4.2 Dependence on the angle of attack

Drag, lift, and moment coefficients, as a function of the angle of attack α, for the first batch of experiments ($h_c = 9.5$), are discussed in this section. Their values are presented in Figure 12 and are compared with the experimental results by Wadlin et al. (1950) and Wadlin et al. (1955). The latter are obtained with a single rectangular NACA 64-A412 hydrofoil. They are also compared with the unbounded flow potential and the RANS numerical simulations by Ocaña Blanco et al. (2017) for the present geometry. Finally, also for the present geometry, results with the classical thin airfoil theory (Münk, 1924) with a correction for free surface effects of the biplane configuration (Glauert, 1948) (Daskovsky, 2000) are included.

Error bars in Figure 12 and in the rest of the paper have

been computed as discussed in Appendix B. The length of these bars is taken as the values of the total uncertainties for each case, shown in Tables B1 – B3 in the appendix. Other than for some particular magnitudes and cases such as c_d for α = 10° in Figure 12, or later on in Figure 15, they are too small to be appreciated in the graphs.

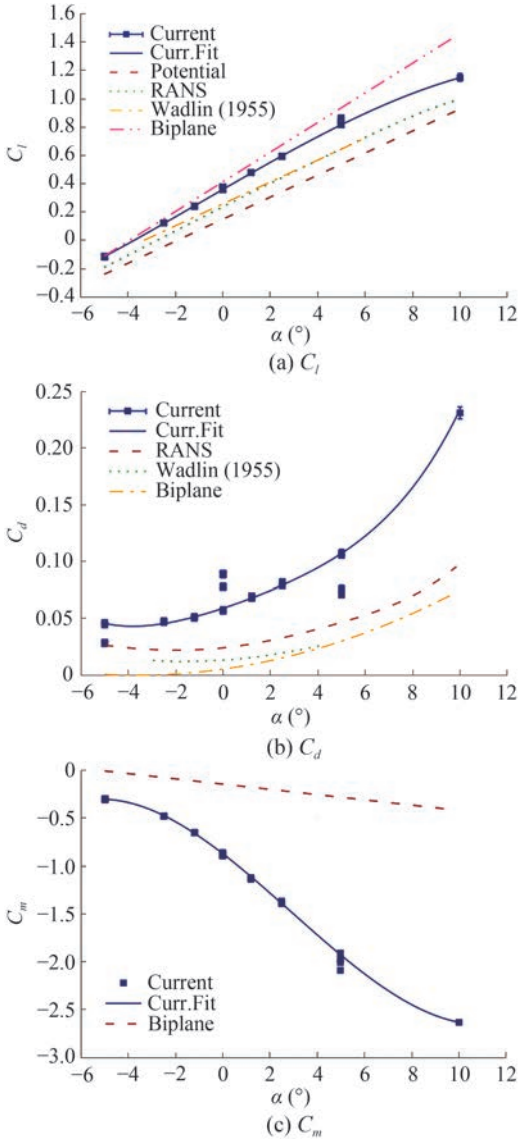

Figure 12 Coefficients for varying α

A brief discussion regarding the dependence of the coefficients on the angle of attack follows:

1) Lift coefficients:

- The experimental lift curve behaves linearly between – 5° and 5° and the slope is slightly reduced from 5° to 10°, which is a reasonable tendency for these curves, as it is also reported by e.g. Ducoin and Young (2013).

- C_l values from (Wadlin et al., 1955) and RANS code are rather similar, a surprising result considering how different the geometries (wing planform, airfoil section, etc.) are.

- The present experimental coefficients are larger than those from (Wadlin et al., 1955), and those from the RANS and potential codes. Due to the large submergence (h_c = 9.5), the presence of the free surface is discarded as an effect to induce any significant difference. Moreover, one expects that they would lead to a reduction in the lift coefficients, not an increase. Hydroelastic effects are not accounted for in the simulations and may have an influence. In Ducoin and Young (2013) a comparison is made between a rigid and a flexible hydrofoil, showing that hydroelastic effects might produce an increase in lift and drag coefficient, which is especially notorious at higher speeds. In addition, experiments are carried out at a range of Reynolds numbers within the laminar-turbulent transition regime. As also documented by Harwood et al. (2016), the lift coefficient is speed-dependent at low speeds, when the Reynolds numbers are $Re \leqslant 5 \times 10^5$ (as in our case). For this range, they report a higher lift coefficient than in the fully turbulent range, which is the one considered by Ocaña Blanco et al. (2017). Finally, the walls of the towing tank can induce some blockage effect, which may cause some increase in the coefficients, as also reported by Ducoin and Young (2013). One qualitative evidence that was noted is the formation of wing shaped tessellations with the dust at the bottom of the tank, which is indicative that the pressure pulses are strong enough so as to lead to some transport in the areas close to the tank bottom and eventually lateral walls. All these comments suggest lines for future work.

- The thin airfoil theory plus the biplane correction yields values quite similar to those obtained in the experiments.

- Overall, the steepness of the lift coefficient curves in Figure 12 are all of the same order of magnitude, something that can be attributed to the fact that NACA 64-A412 and the present NACA 63-210 are similar profiles.

2) Drag coefficients:

- The drag curve exhibits a non-linear (approximately quadratic) behavior.

- C_d values are larger than those of (Wadlin et al., 1955), most probably due to 3D effects coming from the different geometry that is tested and also from the interference of the fuselage.

- The RANS code produces a closer C_d to present experiments than (Wadlin et al., 1955) results. The additional submergence of the mast compared to the one used in the numerical experiments (b_k/c = 2.7) induces some additional friction resistance in the mast. There might be some additional effects due to turbulence modeling and laminar-turbulent transition that are not captured by the codes.

- Thin airfoil theory only captures the induced drag portion of C_d. As expected, these C_d values are lowest ones.

3) Moment coefficient. Unfortunately there are not many available results in literature with configurations similar to those of the experiments. The moment curve is rather linear except for the larger values of angle of attack.

The moment curve slope from thin airfoil theory is around one third of that from the experiments. In any case, the shape and slope of the moment curve is similar to that of a full configuration civilian aircraft (Cui et al., 2021).

In order to use these curves in VPPs, polynomials have been least squares fitted to such curves, with a fair degree of correlation $R^2 > 0.99$. They are presented in Eq. (7):

$$\begin{aligned} C_l(\alpha) &= -0.000\,143\alpha^3 - 0.000\,350\alpha^2 + \\ &\quad 0.966\,669\alpha + 0.359\,405 \\ C_d(\alpha) &= -0.000\,009\alpha^4 - 0.000\,031\alpha^3 + \\ &\quad 0.000\,469\alpha^2 + 0.006\,901\alpha + 0.059\,048 \\ C_m(\alpha) &= 0.001\,129\alpha^3 - 0.009\,817\alpha^2 - \\ &\quad 0.190\,741\,2\alpha - 0.870\,580 \end{aligned} \tag{7}$$

It can be hypothesized that these fitting formulae and the next ones in the paper can be used as a first estimate for modeling these coefficients in state-of-the-art foils for kitefoil and windfoil boards.

Even though the shape of the C_d curve is approximately quadratic with α (and the lift one is approximately linear), since one objective of the paper is to provide accurate values for a VPP, it seems a reasonable idea to provide a fitting which aims to cover the available data. This is the reason for considering higher degree polynomials. The formulae are in any case fast to compute, and can be used in also fast computations such as those required by a VPP.

4.3 Dependence on the submergence

Data from the second batch of experiments have been non-dimensionalized, and the results are presented in Figure 13. In order to better understand them, a fitting of the following type is proposed:

$$C_{[\cdot]}(\alpha, h_c) = C_{[\cdot]}(\alpha, h_c = \infty)\left(1 - 0.5 \cdot \exp\left(-h_c^{k_2}\right)\right) \tag{8}$$

As it stands, the model has the following convenient properties:

1) For $h_c \to \infty$, $C_{[\cdot]}(\alpha, h_c) \to C_{[\cdot]}(\alpha, h_c = \infty)$.

2) For $h_c \to 0$, $C_{[\cdot]}(\alpha, h_c) \to 0.5 \cdot C_{[\cdot]}(\alpha, h_c = \infty)$, which is consistent with the theoretical 2D results from Hough and Moran (1969).

3) The model is smooth in all its dependencies.

4) The free surface effects are concentrated in a small range of h_c of the order of one, as observed in the experiments.

Calculated fits, which render reasonable results, are presented in Eq. (9):

$$\begin{aligned} C_l(\alpha, h_c) &= C_l(\alpha, h_c = \infty)\left(1 - 0.50 \cdot \exp\left(-h_c^{0.75}\right)\right) \\ C_d(\alpha, h_c) &= C_d(\alpha, h_c = \infty)\left(1 - 0.50 \cdot \exp\left(-h_c^{0.40}\right)\right) \\ C_m(\alpha, h_c) &= C_m(\alpha, h_c = \infty)\left(1 - 0.50 \cdot \exp\left(-h_c^{0.90}\right)\right) \end{aligned} \tag{9}$$

It is relevant to assess whether in a more general fitting of the type

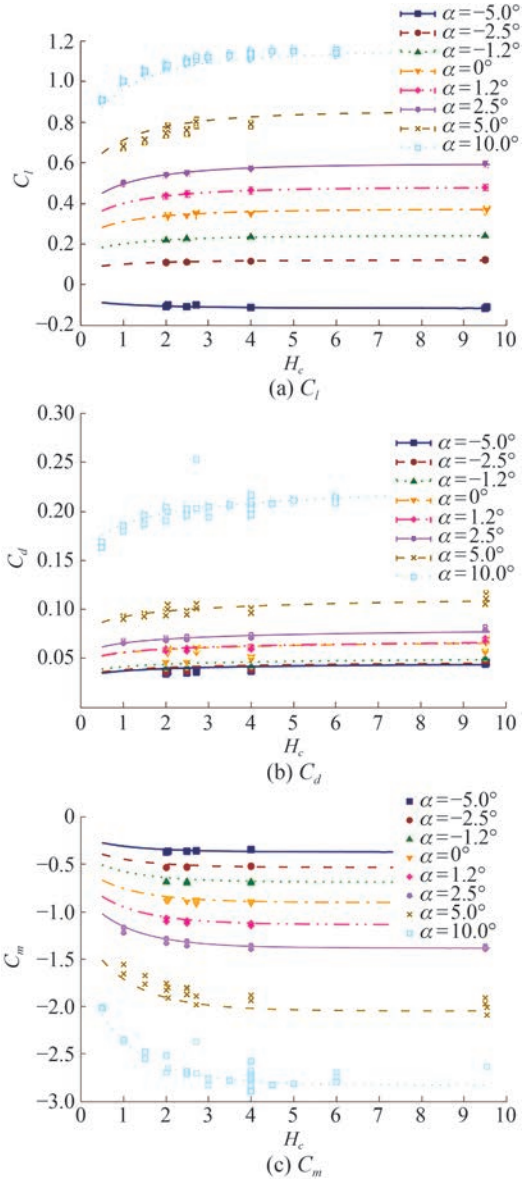

Figure 13 Coefficients for varying α and h_c

$$C_{[\cdot]}(\alpha, h_c) = C_{[\cdot]}(\alpha, h_c = \infty)\left(1 - k_1 \cdot \exp\left(-h_c^{k_2}\right)\right) \tag{10}$$

the constant k_1 is close to 0.5. Results for this latter fitting are presented in Eq. (11). This are the ones used in Figure 13.

$$\begin{aligned} C_l(\alpha, h_c) &= C_l(\alpha, h_c = \infty)\left(1 - 0.45 \cdot \exp\left(-h_c^{0.70}\right)\right) \\ C_d(\alpha, h_c) &= C_d(\alpha, h_c = \infty)\left(1 - 0.50 \cdot \exp\left(-h_c^{0.40}\right)\right) \\ C_m(\alpha, h_c) &= C_m(\alpha, h_c = \infty)\left(1 - 0.45 \cdot \exp\left(-h_c^{0.90}\right)\right) \end{aligned} \tag{11}$$

As can be appreciated, the values of the parameter k_1 for the three coefficients are close to 0.5, as anticipated. Moreover, the shape of the curve C_l/h_c qualitatively agrees with that of Bonnard et al. (2022), who experimentally studied the curve C_l/α for three different submergences ($h_c < 3.3$).

Focusing on Figure 13, the lift coefficient C_l is usually plotted in the form $C_l/C_{l\infty}$ when discussing its dependence on the submergence ratio h_c. It can be noticed that the fitting of Eq. (11) is more accurate for angles of attack $-2.5° \leqslant \alpha \leqslant +5°$. This is not a problem because the actual flying angles are typically within this range.

It is also worth mentioning that the shape of the $C_l/C_{l\infty}$ curves qualitatively agrees with those of Miguel Montero and Minerva (2020), who experimentally studied the range ($h_c < 2.5$) with a nearly constant transverse section hydrofoil.

The shape of the $C_l/C_{l\infty}$ fit can also be compared with the theoretical 2D results. The comparison is presented in Figure 14, where labels Cambered and FlatPlate correspond to the results of Hough and Moran (1969), and label Turnock corresponds to the results of Molland and Turnock (2007). It can be noticed that the shape of the curves is similar to that of theirs, but with a lower $C_l/C_{l\infty}$ coefficient for $h_c < 4$, probably due to the 3D effects in the present geometry. The proposed fitting model achieves a better result than that of Hough and Moran (1969) and Molland and Turnock (2007) compared to the experimental results presented here.

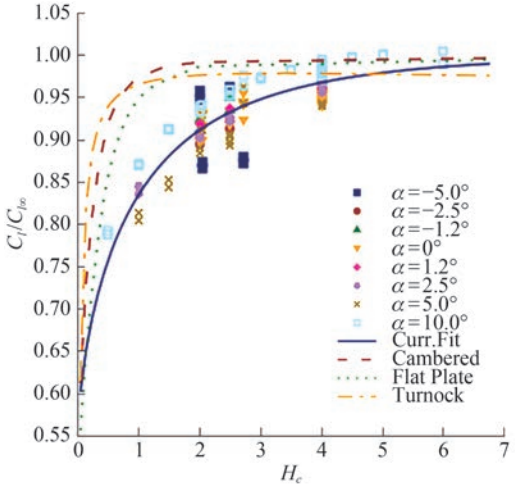

Figure 14 $C_l/C_{l\infty}$ coefficients for varying α and h_c

4.4 Dependence on the Froude number based on submergence

It is relevant to investigate whether Froude number based on submergence, Fr_h, may also play a role when, with the same h_c, the speed of the specimen is increased from its maximum value in the tank (~4 m/s, Fr_c = 4) to actual sailing speeds (~10 m/s, Fr_c = 10).

For example, let us assume h_c = 4 (a typical sailing condition) and α = 0° . For this submergence, Fr_h changes from 2 to 5 if the speed increases from 4 m/s (laboratory conditions) to 10 m/s (actual sailing speed). If the coefficients are plotted with Fr_h as the independent variable (Figure 15), it can be seen that by moving from Fr_h = 2 to Fr_h = 5, around 17% of the lift coefficient is reduced (from 0.36 to 0.30); a similar reduction can also be observed in the drag coefficient (Figure 15).

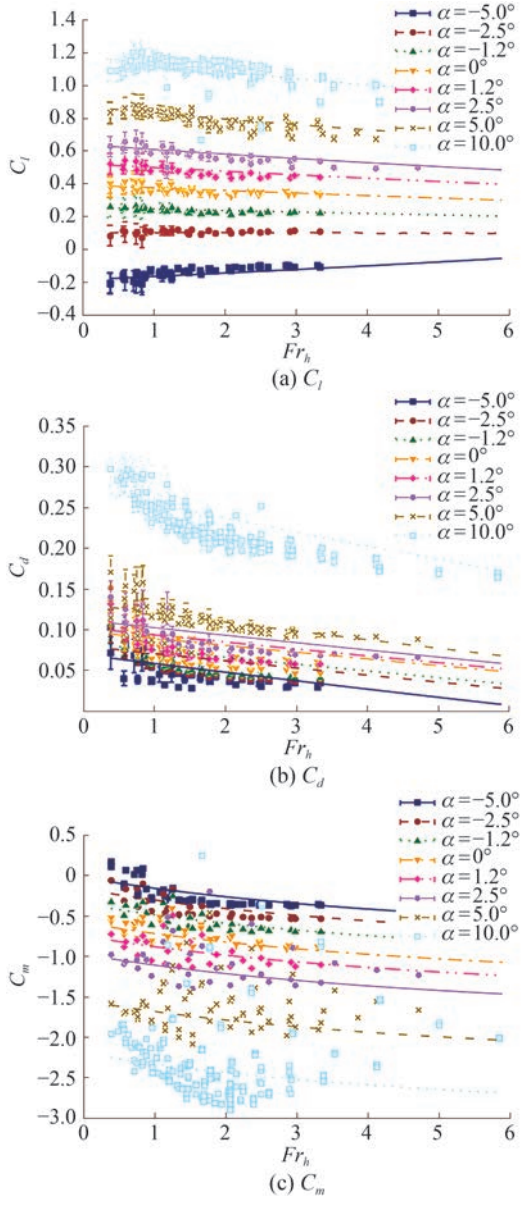

Figure 15 Coefficients for varying Fr_h

The relevance of this estimate is substantial, as it enables the use of data obtained with the limited velocity in the present tests (4 m/s) to actual sailing conditions (10 m/s).

In order to obtain a model for the joint α, h_c and Fr_h dependency, a fitting of the following type is proposed (Eq. (12)):

$$C_{[\cdot]}(\alpha, h_c, Fr_h) = C_{[\cdot]}(\alpha, h_c, Fr_h = 0.4) - \left(1 - \frac{1}{1 - k_{C_{[\cdot]}} \cdot Fr_h}\right) \tag{12}$$

Similarly to the submergence dependence analysis, Fr_h = 0.4 is used as a reference in Eq. (12) as it corresponds to

the value of the deepest submergence tested.

The factor $k_{C_{[]}}$ in Eq. (12) has been fitted using a second-order polynomial, with a fair degree of correlation, $R^2 > 0.99$ for C_l and $R^2 > 0.93$ for C_d. These fittings are shown next (Eq. (13)):

$$\begin{aligned} k_{C_l} &= -0.000\,27\alpha^2 + 0.006\,02\alpha + 0.017\,05 \\ k_{C_d} &= 0.000\,10\alpha^2 + 0.000\,05\alpha + 0.008\,71 \\ k_{C_m} &= 0.140\,00 \end{aligned} \tag{13}$$

5 Conclusions and future work

In this paper, an experimental investigation on the hydrodynamics of a full-scale state-of-the-art hydrofoil (suitable both for kitesurf and windsurf) has been documented. The experiments were carried out in the towing tank of ETSIN, "Universidad Politécnica de Madrid (UPM)", Spain. During the experiments, forces and torques produced, under uniform flow, were measured, and related non-dimensional coefficients were estimated. Various parameters were varied: first, a range of velocities up to 4 m/s (Reynolds based on the mean chord is 2.9×10^5) was tested, relative angular positions with respect to the advance speed, with attack angles ranging from −5 to 10 degrees, were also tested, and finally, the submergence was changed in the tests from deep-water conditions to cases near the free surface, implying that tests were carried out for a range of Froude numbers based on submergence with maximum values around five. This is a typical range in actual sailing conditions, allowing estimations of the coefficients for higher actual speeds than the ones allowed by the towing tank carriage. To the authors' knowledge no such results are available for a low aspect 3D foil such as the one studied in the paper. When compared with high-aspect ratio foils from the literature, significant differences have been found, such as the present foil showing slightly higher lift and substantially higher drag. From these tests, formulae for the hydrodynamic coefficients, including their dependence on the Froude number based on submergence, have been proposed. The correlations in the formulae are 0.99 for C_l and 0.93 for C_d. With this accuracy, the authors think that such formulae can be used for developing VPP for this kind of crafts, a necessary tool to plan racing configurations and to analyze the racing performance of the craft. This is part of our future work, which will also include tests at sea using this same specimen, with a monitoring device providing information on speed, attitude, distance to water, and motions. Future work will also include studying ventilation and transition to turbulence. Finally, with the aim of making the experimental data useful for benchmarking numerical models, the specimen 3D file is provided as supplementary material to this paper.

Appendix A Torque measurement point

First, in Figure A1 the length and surface of the mast are shown.

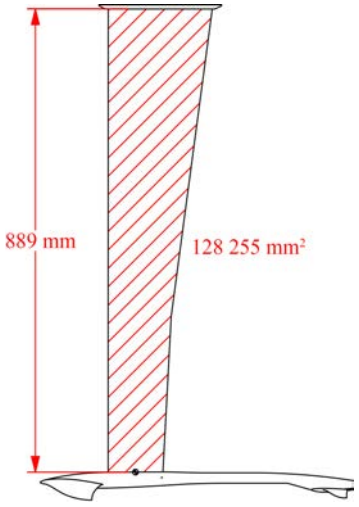

Figure A1 Mast length and surface

Coordinates of the points where torques were measured are shown in Figures A2–A5.

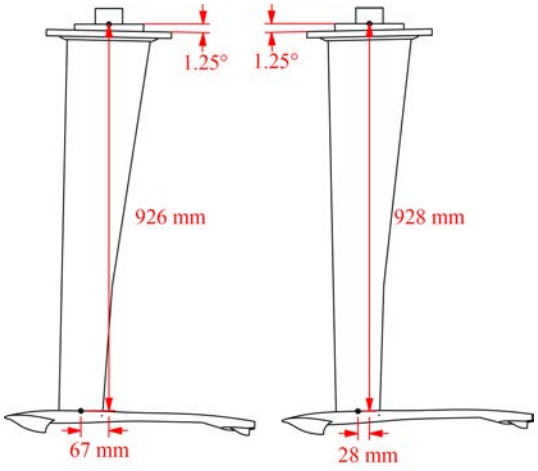

Figure A2 Coordinates of the points where torques are measured for $\alpha = \pm 1.25°$

Appendix B Notes on experimental uncertainty

In this campaign, the force coefficient C_i in the $i = 1, 2, 3$, corresponding to x, y, z directions, respectively, is defined as presented in Eq. (3), with the variables involved defined in Table 1. Verification of the calibration of moments was out of the scope of the present campaign, and therefore the uncertainty assessment for the data of M_y, the only moment considered in the present study, is left for future work.

The analysis will be carried out according to the ITTC recommendations as presented in the general principles of

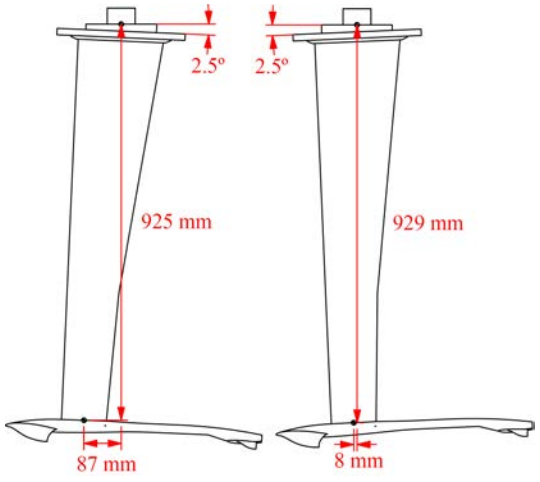

Figure A3 Coordinates of the points where torques are measured for $\alpha = \pm 2.5°$

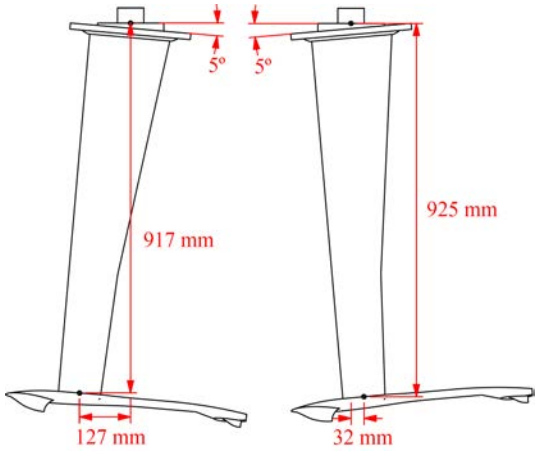

Figure A4 Coordinates of the points where torques are measured for $\alpha = \pm 5°$

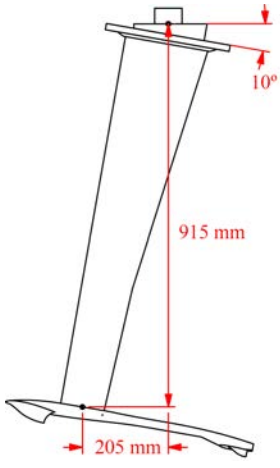

Figure A5 Coordinates of the points where torques are measured for $\alpha = 10°$

(ITTC, 2014b) and the example corresponding to the total resistance coefficient documented in (ITTC, 2017a).

Following such general principles (ITTC, 2014b), the uncertainty in C_i is obtained by propagating those of the variables involved in the corresponding formula, with the proportionality coefficients being the partial derivatives with respect to each variable, i.e:

$$u^2(C_i) = \left(\frac{2}{\rho u_\infty^2 S}\right)^2 u^2(F_i) + \left(\frac{-4F_i}{\rho u_\infty^3 S}\right)^2 u^2(u_\infty) + \left(\frac{-2F_i}{\rho u_\infty^2 S^2}\right)^2 u(S)^2 \quad \text{(B1)}$$

The contribution of density is not included in the formula as its own uncertainty, multiplied by its corresponding factor, is negligible.

In order to better understand the procedure to estimate these terms, let us take as an example the case of the drag coefficient, C_1, for $h_c = 4$ and $\alpha = \beta = \gamma = 0°$, $V = 4$ m/s. This is an interesting choice, as it corresponds to tailwind navigation conditions, a common one. In addition, the speed is the highest allowed in the tank and, therefore, is the closest to the operational one. Finally, the submergence is a typical one, according to feedback provided by experienced riders.

In this case, the number of repetitions is $N = 11$, which is a reasonable choice following (ITTC, 2017b), and includes tests conducted on two different days. The standard deviations of forces and velocities obtained from this case will be used to estimate those for other cases where no repetitions were performed.

Regarding the uncertainties in the forces, they will be divided into A (repetition related) and B (calibration) types:

$$u^2(F_i) = u_A^2(F_i) + u_B^2(F_i) \quad \text{(B2)}$$

The A-type uncertainty is obtained from analyzing the repeatability of the experiments, estimated from repeated measurements using the expression (ITTC, 2014a):

$$u_A(F_i) = \frac{\sigma}{\sqrt{N}} \quad \text{(B3)}$$

with σ being the standard deviation of the force values obtained in the repeated tests, and N the number of repeated tests. Following (ITTC, 2014a), the standard deviation is obtained using the classic unbiased discrete estimate:

$$\sigma = \sqrt{\frac{1}{N-1}\sum_{j=1}^{N}\left(\hat{F}_i^j - F_i\right)^2} \quad \text{(B4)}$$

with $\hat{F}_i^j$ obtained with the mean value (in time) of the force in the direction i in test j, and F_i is the mean value of those $\hat{F}_i^j$.

In the particular case of the proposed example, $F_1 = 24.07$ N, $\sigma = 0.541$ N and therefore $u_A(F_1) = 0.163$ N.

As an example, the time histories of the forces measured during two repetitions are presented in Figure B1.

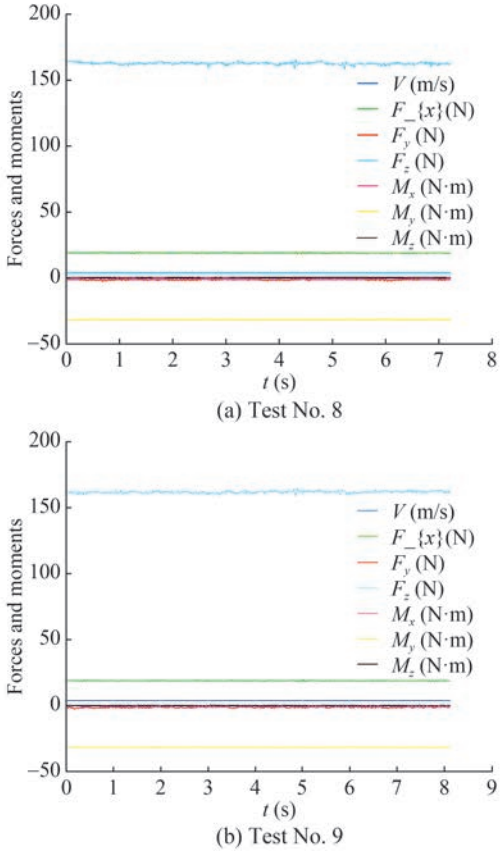

Figure B1 Time histories of forces and moments for two repeated tests for uncertainty analysis

Regarding the B-type uncertainty for the forces, the force/torque sensor used was a 6DOF ATI Industrial Automation model Mini58 IP65/IP68. Its ranges are 2 800 N for F_1 and F_2, 6 800 N for F_3 and 120 N·m for the three torques. Considering that the x-force leads to a substantial M_y moment, the torque range is the limiting factor when it comes to increasing the speed or the angle of attack. In order to be able to measure such a moment, it was hence necessary to use a sensor with larger force ranges than the ones found in the actual physics of the present phenomenon.

For this reason, the force/torque sensor was calibrated, using static measurements, for the specific range of the forces and moment of these tests. The standard deviations of the residuals of such recalibration are taken as the $u_B(F_i)$ uncertainty, with $i = 1, 2, 3$ for the x, y, z directions:

$$u_B(F_1) = 0.079\,6 \text{ N}, u_B(F_2) = 0.067\,6 \text{ N}, \\ u_B(F_3) = 0.919\,7 \text{ N} \tag{B5}$$

Therefore, applying Eq. (B2), one gets for the proposed example $u(F_1) = 0.181$ N, with a larger contribution from the A-type uncertainty.

Concerning the uncertainty due to speed, the carriage's control system provides average velocity values within ±1 mm/s absolute precision, which, assuming a constant probability distribution, results in:

$$u_B(u_\infty) = \frac{0.001}{\sqrt{3}} = 5.8 \times 10^{-4} \text{ m/s} \tag{B6}$$

with $u_A(u_\infty) = 6.7 \times 10^{-5}$ m/s, obtained analogously to $u_A(F_1)$, leading to $u(u_\infty) = 5.8 \times 10^{-4}$ m/s.

As for the geometry, the associated uncertainty is determined assuming length errors not larger than 1 mm, projected on the span of the unit, leading to:

$$u(S) = 6.5 \times 10^{-4} \text{ m}^2 \tag{B7}$$

With this uncertainty, our aim is to account for the impact of the deviation (which is unknown beyond that precision) between the CAD file and the actual specimen.

Summarizing, for this example, in which $C_1 = 0.051\,1$, applying Eq. (B1), one gets $u(C_1) = 8.3 \times 10^{-4}$, and the relative one $u'(C_1) = u(C_1)/C_1 = 0.016$.

With a coverage factor $k = 2$ (ITTC, 2014b), one finds that the total uncertainty U is:

$$U(C_1) = k \cdot u(C_1) \tag{B8}$$

which for this case renders $U(C_1) = 1.67 \times 10^{-3}$.

This can be written as: $C_1 = 0.051\,09 \pm 0.001\,67$, or $C_1 = 0.051\,09 \pm 3.3\%$.

The largest contribution to the total uncertainty in Eq. (B1) for this case is the one due to geometry.

The uncertainty $U(C_i)$ is calculated for each case and for each direction and is used to determine the magnitude of the error bars in the curves displaying these variables. As aforementioned, the standard deviations of forces and velocities obtained for the sample case considered in this section have been used to compute u_A of forces and velocities for other cases for which no repetitions were made, obviously not reduced by the square root of the number of repetitions in Eq. (B3). In Tables B1–B3 the values of C_l, C_d, the standard deviations of their time history averages, and their uncertainties, for the cases considered for the proposed C_l and C_d fitting formulae ($3.5 \leqslant u_\infty \leqslant 4.0$, u_∞ in m/s), have been included. The number of repeated tests, N, done for each case (α, h_c, u_∞) has also been included in the tables ($N = 1$ implies that no repetition was done).

Table B1 Uncertainties of the cases considered for the proposed C_l and C_d fitting formulae, $-5° \leqslant \alpha \leqslant -1.25°$

α	h_c	u_∞	N	C_l	$U(C_l)$	C_d	$U(C_d)$
−5	2	3.5	2	−0.1034	0.0056	0.0368	0.0019
−5	2	4	2	−0.1035	0.0045	0.0350	0.0015
−5	2.5	3.5	2	−0.1043	0.0056	0.0372	0.0019
−5	2.5	4	2	−0.1042	0.0045	0.0355	0.0015

Table B1 Uncertainties of the cases considered for the proposed C_l and C_d fitting formulae, $-5° \leqslant \alpha \leqslant -1.25°$ (Continued)

α	h_c	u_∞	N	C_l	$U(C_l)$	C_d	$U(C_d)$
−5	4	3.5	1	−0.1110	0.0057	0.0387	0.0019
−5	4	4	1	−0.1103	0.0046	0.0365	0.0015
−5	9.5	3.5	2	−0.1145	0.0057	0.0465	0.0020
−5	9.5	4	2	−0.1126	0.0046	0.0446	0.0016
−2.5	2	3.5	1	0.1086	0.0056	0.0383	0.0019
−2.5	2	4	1	0.1095	0.0046	0.0362	0.0015
−2.5	2.5	3.5	1	0.1107	0.0057	0.0388	0.0019
−2.5	2.5	4	1	0.1118	0.0046	0.0370	0.0015
−2.5	4	3.5	1	0.1162	0.0057	0.0406	0.0019
−2.5	4	4	1	0.1167	0.0047	0.0388	0.0015
−2.5	9.5	3.5	1	0.1206	0.0058	0.0481	0.0020
−2.5	9.5	4	1	0.1221	0.0047	0.0462	0.0016
−1.25	2	3.5	1	0.2202	0.0070	0.0422	0.0019
−1.25	2	4	1	0.2228	0.0063	0.0406	0.0016
−1.25	2.5	3.5	1	0.2257	0.0071	0.0427	0.0019
−1.25	2.5	4	1	0.2292	0.0064	0.0411	0.0016
−1.25	4	3.5	1	0.2340	0.0073	0.0441	0.0019
−1.25	4	4	1	0.2387	0.0066	0.0426	0.0016
−1.25	9.5	3.5	1	0.2415	0.0074	0.0518	0.0020
−1.25	9.5	4	1	0.2407	0.0066	0.0500	0.0017

Table B2 Uncertainties of the cases considered for the proposed C_l and C_d fitting formulae, $0° \leqslant \alpha \leqslant 2.5°$

α	h_c	u_∞	N	C_l	$U(C_l)$	C_d	$U(C_d)$
0	2	4	5	0.3393	0.0085	0.0558	0.0018
0	2	3.5	2	0.3346	0.0090	0.0583	0.0021
0	2.5	4	5	0.3489	0.0087	0.0566	0.0018
0	2.7	3.5	3	0.3454	0.0092	0.0598	0.0021
0	4	4	11	0.3491	0.0087	0.0511	0.0017
0	9.5	4	5	0.3708	0.0091	0.0660	0.0020
0	9.5	3.5	3	0.3643	0.0096	0.0649	0.0023
1.25	2	3.5	1	0.4354	0.0109	0.0592	0.0021
1.25	2	4	1	0.4403	0.0105	0.0576	0.0018
1.25	2.5	3.5	1	0.4441	0.0110	0.0601	0.0021
1.25	2.5	4	1	0.4491	0.0106	0.0581	0.0018
1.25	4	3.5	1	0.4615	0.0114	0.0617	0.0021
1.25	4	4	1	0.4657	0.0110	0.0599	0.0018
1.25	9.5	3.5	1	0.4793	0.0117	0.0702	0.0023
1.25	9.5	4	1	0.4791	0.0113	0.0677	0.0020
2.5	1	3.5	1	0.4964	0.0121	0.0678	0.0022
2.5	1	4	1	0.5018	0.0117	0.0658	0.0019
2.5	2	3.5	1	0.5359	0.0129	0.0706	0.0023
2.5	2	4	1	0.5398	0.0125	0.0685	0.0020
2.5	2.5	3.5	1	0.5476	0.0131	0.0719	0.0023
2.5	2.5	4	1	0.5513	0.0128	0.0697	0.0020
2.5	4	3.5	1	0.5687	0.0135	0.0737	0.0023
2.5	4	4	1	0.5725	0.0132	0.0716	0.0020
2.5	9.5	3.5	1	0.5927	0.0140	0.0818	0.0025
2.5	9.5	4	1	0.5954	0.0137	0.0792	0.0022

Table B3 Uncertainties of the cases considered for the proposed C_l and C_d fitting formulae, $5° \leqslant \alpha \leqslant 10°$

α	h_c	u_∞	N	C_l	$U(C_l)$	C_d	$U(C_d)$
5	1	3.5	1	0.6736	0.0157	0.0926	0.0026
5	1	4	1	0.6808	0.0155	0.0900	0.0024
5	1.5	3.5	1	0.7053	0.0164	0.0956	0.0027
5	1.5	4	1	0.7130	0.0162	0.0929	0.0024
5	2	3.5	2	0.7509	0.0176	0.1011	0.0028
5	2	4	2	0.7611	0.0176	0.0970	0.0025
5	2.5	3.5	3	0.7638	0.0181	0.1005	0.0029
5	2.5	4	3	0.7720	0.0182	0.0971	0.0026
5	4	3.5	1	0.7864	0.0181	0.1011	0.0028
5	4	4	1	0.7887	0.0178	0.0968	0.0025
5	9.5	3.5	2	0.8308	0.0193	0.1116	0.0030
5	9.5	4	2	0.8426	0.0194	0.1081	0.0028
10	0.5	3.5	4	0.9091	0.0206	0.1661	0.0041
10	1	3.5	3	1.0022	0.0227	0.1837	0.0044
10	1.5	3.5	4	1.0501	0.0237	0.1916	0.0046
10	2	3.5	4	1.0784	0.0244	0.1997	0.0047
10	2.5	3.5	6	1.1052	0.0248	0.2089	0.0048
10	3	3.5	3	1.1198	0.0252	0.2011	0.0048
10	3.5	3.5	2	1.1303	0.0255	0.2064	0.0048
10	4	3.5	15	1.1305	0.0257	0.2042	0.0049
10	4.5	3.5	2	1.1482	0.0258	0.2085	0.0049
10	5	3.5	2	1.1513	0.0259	0.2110	0.0049
10	6	3.5	4	1.1478	0.0260	0.2119	0.0050
10	9.5	3.5	1	1.1505	0.0259	0.2272	0.0053

Competing interest A. Souto-Iglesias is an editorial board member for the Journal of Marine Science and Application and was not involved in the editorial review, or the decision to publish this article. All authors declare that there are no other competing interests.

References

Angelou M, Spyrou KJ (2019) Modeling of transient hydrodynamic lifting forces of sailing yachts and study of their effect on maneuvering in waves. Ocean Engineering 173: 531-547. https://doi.org/10.1016/j.oceaneng.2019.01.021

Barden T, Binns J (2012) On the road to establishing ventilation probability for moth sailing dinghies. 18th Australasian Fluid Mechanics Conference, Launceston, Australia, 1-4

Beaver B, Zseleczky J (2009) Full scale measurements on a hydrofoil international moth. 19th Chesapeake SailingYacht Symposium, Annapolis, USA, SNAME-CSYS-2009-013. https://doi.org/10.5957/CSYS-2009-013

Binns J, Brandner P, Plouhinec J (2008) The effect of heel angle and free-surface proximity on the performance and strut wake of a moth sailing dinghy rudder t-foil. High Performance Yacht Design Conference, Auckland, New Zealand, 121-129

Bonnard H, Chatellier L, David L (2022) Investigation of 3D effects and free-surface proximity influence on the flow around a hydrofoil using piv measurements. 20th International Symposium on Applications of Laser and Imaging Techniques to Fluid Mechanics,

Lisbon, Portugal, 1-9. https://hal.science/hal-03873831
Campbell I, Owen M, Provinciali G (2014) Dagger-board evaluation for an imoca 60 yacht. Ocean Engineering 90: 2-10
Carter AW, Butler RV (1953) Experimental investigation of the flow field behind an aspect-ratio-10 hydrofoil near the water surface. National Advisory Committee for Aeronautics, Washington, United States, Report Number NACA-RM-L52L11
Cui X, Zhou Z, Yu Y, Yu L, Li Y, Zhou T (2021) Numerical analysis and improvement of longitudinal moment pitch-up characteristics for civil aircraft. Journal of Physics: Conference Series 2010(1): 012075. DOI: 10.1088/1742-6596/2010/1/012075
Daskovsky M (2000) The hydrofoil in surface proximity, theory and experiment. Ocean Engineering 27(10): 1129-1159
Day S, Cocard M, Troll M (2019) Experimental measurement and simplified prediction of t-foil performance for monohull dinghies. 23rd Chesapeake Sailing Yacht Symposium, Annapolis, USA
Ducoin A, Young YL (2013) Hydroelastic response and stability of a hydrofoil in viscous flow. Journal of Fluids and Structures 38: 40-57
Giallanza A, Marannano G, Morace F, Ruggiero V (2020) Numerical and experimental analysis of a high innovative hydrofoil. International Journal on Interactive Design and Manufacturing 14: 43-57
Glauert H (1948) The elements of aerofoil and airscrew theory. Cambridge University Press, Cambridge, UK. https://doi.org/10.1017/CBO9780511574481
Gómez Tierno MA, Pérez Cortés M, Puentes Márquez C (2012) Mecánica del vuelo. Garceta Grupo Editorial, Madrid, Spain. (in Spanish)
Harwood CM, Young YL, Ceccio SL (2016) Ventilated cavities on a surface-piercing hydrofoil at moderate Froude numbers: Cavity formation, elimination and stability. Journal of Fluid Mechanics 800: 5-56
Hough G, Moran J (1969) Froude number effects on two dimensional hydrofoils. Journal of Ship Research 13(1): 53-60
ITTC (2014a) General guideline for uncertainty analysis in resistance tests. International Towing Tank Conference, Copenhagen, Denmark, Technical Report No. 7.5-02-02-02
ITTC (2014b) Guide to the expression of uncertainty in experimental hydrodynamics. International Towing Tank Conference, Copenhagen, Denmark, Technical Report No. 7.5-02-01-01, Revision 02
ITTC (2017a) ITTC quality system manual, recommended procedures and guidelines, guideline to practical implementation of uncertainty analysis. International Towing Tank Conference, Wuxi, China, Technical Report No. 7.5-02-01-07
ITTC (2017b) ITTC quality system manual, recommended procedures and guidelines, procedure: Seakeeping experiments. International Towing Tank Conference, Wuxi, China, Technical Report No. 7.5-02-07-02.1
Jentzsch M, Dahms J, Woszidlo R, Nayeri CN, Paschereit CO (2022) Free surface effects and the utility of a skim plate for experiments in a water towing tank at steady and unsteady model velocity. Experiments in Fluids 63: 164. https://doi.org/10.1007/s00348-022-03502-w
Marimon Giovannetti L, Farousi A, Ebbesson F, Thollot A, Shiri A, Eslamdoost A (2022) Fluid-structure interaction of a foiling craft. J. Marine Science and Engineering 10(3): 372
Miguel Montero F, Minerva L (2020) Experimental methods for investigation of foiling crafts. 26th International HISWA Symposium on Yacht Design and Yacht Construction, 1-32
Molland AF, Turnock SR (2007) Marine rudders and control surfaces: Principles, data, design and applications. Butterworth Heinemann, Oxford, UK. DOI: 10.1016/B978-0-7506-6944-3.X5000-8
Münk MM (1924) Elements of the wing section theory and of the wing theory. National Advisory Committee for Aeronautics, Washington, United States, NACA Technical Report No. 191
Ni Z, Dhanak M, Su TC (2021) Performance of a hydrofoil operating close to a free surface over a range of angles of attack. International Journal of Naval Architecture and Ocean Engineering 13: 1-11
Ocaña Blanco D, Castaneda-Sabadell I, Souto-Iglesias A (2017) CFD and potential flow assessment of the hydrodynamics of a kitefoil. Ocean Engineering 146: 388-400
Souppez JB, Dewavrin JM, Gohier F, Labi GB (2019) Hydrofoil configurations for sailing superyachts: Hydrodynamics, stability and performance. Design & Construction of Super & Mega Yachts, Genoa, Italy
Tisserand C (2005) Des hydrofoils a la portée de tous. Available from http://www.voiles-alternatives.com/documents/divers/des_Hydrofoils_a_la_portee_de_tous. pdf [Accessed on May 29, 2025] (in French)
Vanilla T, Benoit A, Benoit P (2021) Hydro-elastic response of composite hydrofoil with FSI. Ocean Engineering 221: 108230
Vellinga R (2009) Hydrofoils: Design, build, fly. Peacock Hill Publishing, Tacoma, United States
Wadlin KL, Ramsen JA, McGehee JR (1950) Tank tests at subcavitation speeds of an aspect-ratio-10 hydrofoil with a single strut. National Advisory Committee for Aeronautics, Washington, United States, NACA Technical Report No. RM L9K14a
Wadlin KL, Shuford Jr CL, McGehee JR (1955) A theoretical and experimental investigation of the lift and drag characteristics of hydrofoils at subcritical and supercritical speeds. National Advisory Committee for Aeronautics, Washington, United States, NACA Technical Report No. NACA-TR-1232
Wang J, Santhosh S, Colomés O, Capaldo M, Yang L (2023) Experimental study of dynamic response of passive flapping hydrofoil in regular wave. Physics of Fluids 35(7): 077127. https://doi.org/10.1063/5.0157890